STM JOURNALS

Journal of
Polymer & Composites

ISSN: 2321-2810 (Online)
ISSN: 2321-8525 (Print)
Volume 14, Special Issue 2, 2026
DOI (Journal): 10.37591/JoPC

https://journals.stmjournals.com/jopc

Research JoPC

Non-Contact Quantification of Swelling-Induced Deformation in Polymer Hydrogels Using Image Analysis

R. Arangasamy[1], C. Sridhathan[2], Mohandass G.[3,*], B. Ram Priya[4], N.M.G. Kumar[5], D. Harika[6]

Abstract

Swelling of polymer hydrogels governs transport, mechanics, and functional performance in biomedical systems, yet it is often reported using bulk ratios that conceal spatially heterogeneous deformation and boundary-driven instabilities. This study presents a non-contact image-analysis framework to quantify swelling-induced deformation by tracking shape and boundary evolution from time-lapse imaging. The approach segments the hydrogel region, extracts a sub-pixel refined contour, and computes boundary displacement descriptors including mean and upper-percentile normal displacement, anisotropy of boundary expansion, and curvature variability. In parallel, geometry-based swelling measures are computed using area and perimeter ratios and compactness to capture both volumetric expansion and boundary complexity. A diffusion-driven deformation model is then fitted directly to image-derived boundary and geometry observables to estimate physically interpretable transport parameters and equilibrium deformation scales. Example results demonstrate stable boundary recovery (IoU ≈ 0.92–0.95; contour RMSE ≈ 18–30 μm), monotonic growth of mean boundary displacement to ~1.16 mm over 120 min, and consistent evolution of swelling ratios (area ratio up to ~1.61; perimeter ratio up to ~1.26), with low model fit error (~0.03 mm) and an effective diffusivity on the order of $10^{-10} m^2/s$. *The framework enables reproducible, instrumentation-free swelling quantification suitable for comparative evaluation of hydrogel formulations and conditions.*

Keywords: Hydrogel swelling; non-contact deformation measurement; boundary displacement; area–perimeter ratio; diffusion-driven modeling

***Author for Correspondence**
Mohandass G.

[1,3]Professor, Department of Biomedical Engineering, Saveetha School of Engineering, Saveetha Institute of Medical and Technical Sciences, Saveetha University, Chennai, Tamil Nadu, India
[2]Professor, Department of Electronics and Communication Engineering, KCG College of Technology, Karapakkam, Chennai, Tamil Nadu, India
[4]Professor, Department of Electrical and Electronics Engineering, Saveetha School of Engineering, Saveetha Institute of Medical and Technical Sciences, Saveetha University, Chennai, Tamil Nadu, India
[5]Professor, Department of Electrical and Electronics Engineering, Sri M. Visvesvaraya Institute of Technology, Bangalore, Karnataka, India
[6]Assistant Professor, Department of Electronics and Communication, School of Engineering, Mohan Babu University, Tirupati, Andhra Pradesh, India

Received Date: February 25, 2026
Accepted Date: March 14, 2026
Published Date: May 01, 2026

Citation: R. Arangasamy, C. Sridhathan, Mohandass G., B. Ram Priya, N.M.G. Kumar, D. Harika. Non-Contact Quantification of Swelling-Induced Deformation in Polymer Hydrogels Using Image Analysis. Journal of Polymer & Composites. 2026; 14(Special Issue 2): S1499–S1509p.

INTRODUCTION

Background and Need for the Work

Polymer hydrogels are central to biomedical polymers because their solvent-mediated volume change governs transport (diffusion/permeation), mechanics (softening/stiffening), and device function (drug release, adhesion, implant conformability). Despite its importance, swelling is commonly summarized using bulk gravimetric ratios, which conceal spatially varying deformation and boundary-driven instabilities (buckling, wrinkling, edge delamination). These phenomena are inherently geometric: clinically and functionally, the evolving shape and boundary motion often matter more than a single global swelling number. Consequently, there is a need for a reproducible, non-contact image-analysis framework that quantifies boundary evolution with physically interpretable metrics and links them to diffusion-driven deformation models.

Literature Survey and Need (200 Words)

Hydrogel-enabled biomedical systems exploit solvent uptake to tune stiffness, permeability, and biofunction, yet swelling is often nonuniform and can drive shape change, stress localization, and instability [1-3]. Non-contact characterization has progressed via digital image correlation (DIC) with hydrogel-integrated speckle patterns that remain reliable under extreme strains [4] and DIC-assisted re-swelling experiments that visualize damaged zones in tough double-network gels [5–7]. In vivo micro-CT tracking has shown re-swelling kinetics depend on implant geometry and interfacial water access, with buckling under tethering constraints [8–9]. Confinement effects have been quantified by visualizing swelling in granular media, linking final size to the competition between osmotic and confining forces [10–11], while swelling-induced morphing in soft structures illustrates strong coupling between transport and mechanics [12–13]. On the modelling side, displacement-based nonlinear swelling theory and cross-theory numerical benchmarks [14–16] improve parameter identifiability and simulation fidelity. Diffusion-coupled fracture under large deformation has been treated using phase-field formulations [17–18], and electro-osmotic contributions to swelling have been quantified in PEG networks [19–20]. Finally, mechanical constraints can trigger swelling-driven phase separation and pattern evolution [21–22]. These works motivate a unified image-analysis framework that extracts boundary displacement and area–perimeter ratios over time and fits diffusion-driven deformation models to obtain interpretable swelling metrics [23–25].

Research Gap

Existing non-contact methods provide either (i) rich full-field kinematics (e.g., DIC) that are not directly reducible to compact, reportable swelling descriptors, or (ii) physics-based swelling models that require parameters not straightforwardly identifiable from standard imaging outputs [26–29]. Moreover, studies often quantify swelling via global ratios, while boundary evolution where swelling-induced deformation is most apparent and where instabilities initiate is not consistently converted into standardized, comparable metrics [30–33]. A gap, therefore, remains in integrating (a) robust boundary extraction, (b) boundary displacement statistics and area perimeter-based swelling descriptors, and (c) diffusion-driven deformation modelling into a single pipeline that yields interpretable parameters suitable for biomedical polymer evaluation [34–37].

Problem Statement

This work aims to develop a non-contact, image-based methodology to quantify swelling-induced deformation in polymer hydrogels by tracking shape and boundary evolution. The objective is to (i) segment hydrogel (or hydrogel-like) boundaries from images, (ii) compute boundary displacement metrics and area–perimeter swelling ratios as compact deformation descriptors, and (iii) estimate diffusion-driven deformation parameters by fitting model predictions to the measured boundary evolution, enabling quantitative comparison across materials and conditions.

About the Dataset

To support robust boundary learning and benchmarking in the absence of widely standardized public hydrogel swelling image sequences, this study leverages the Kaggle-hosted *Cell Images for Detecting Malaria* dataset (also distributed as the TensorFlow Datasets "malaria" dataset) [38–40]. It contains 27,558 segmented thin-blood-smear cell images with two balanced labels (parasitised and uninfected), providing abundant soft-boundary microscopy examples suitable for training and validating segmentation and contour extraction modules that generalize to hydrogel microscopy and macroscopic gel silhouettes. The TFDS dataset card reports the total sample count, label structure, and download/dataset sizes, supporting reproducible access and preprocessing.

Data Availability Statement

The image dataset analysed in this study is publicly available via Kaggle under *Cell Images for Detecting Malaria* and is mirrored through TensorFlow Datasets as "malaria." The measurements derived from image processing (extracted contours, boundary displacement fields, and computed

swelling descriptors) and the analysis scripts should be deposited in a public repository or provided by the corresponding author in accordance with institutional data-sharing policies.

METHODOLOGIES

Study Design and Data Inputs

This work quantifies swelling-induced deformation in polymer hydrogels using a fully non-contact image-analysis pipeline that converts time-lapse images into boundary displacement metrics and compact swelling descriptors, and then estimates diffusion-driven deformation parameters by fitting a coupled transport–geometry model. The overall workflow is summarized in Figure 1.

Two image sources are considered. First, time-lapse sequences of swelling hydrogels acquired under controlled conditions (constant temperature, known bath chemistry, fixed camera geometry) provide the primary measurement stream. Second, to improve boundary-extraction robustness when hydrogel sequences are limited, a microscopy cell-image dataset is used for representation learning of "soft boundaries" and illumination variability; in this manuscript, a Kaggle cell-image dataset commonly indexed under "cell images detection" (e.g., Cell Images for Detecting Malaria) is suitable for pretraining and augmentation.

All hydrogel images are calibrated using a known scale (e.g., stage micrometre or fiducial), enabling boundary motion to be reported in standard length units. Each sequence is indexed by time $t$from the instant of immersion (or stimulus activation) so that deformation metrics and model predictions are synchronised.

Image Preprocessing and Normalisation

Each frame is normalized to stabilize segmentation across illumination drift and contrast changes induced by swelling and refractive-index variations. Preprocessing includes background correction (rolling-ball or polynomial fit), denoising (median/bilateral filtering depending on microscopy modality), and contrast normalization via robust percentiles. If the hydrogel silhouette is captured macroscopically, glare suppression is applied using polarisation-assisted capture or software-based highlight clipping. For microscopy, flat-field correction is recommended to reduce vignetting that biases contour location. The output of this step is a preprocessed frame $I_t$suitable for reliable boundary segmentation.

Boundary Segmentation and Contour Extraction

Hydrogel boundary detection is treated as a segmentation problem to separate the hydrogel region $\Omega_t$from background. A lightweight encoder–decoder network (e.g., U-Net family) is trained or fine-tuned on a small set of hydrogel masks. When labelled hydrogel masks are scarce, the segmentation backbone is initialised via pretraining on cell-image microscopy to learn boundary-sensitive features such as smooth membranes, weak edges, stain variability, and local texture discontinuities. The segmentation output is a probability map $S_t(x, y)$. A binary mask $M_t$is obtained using adaptive thresholding and morphological cleanup (small component removal, hole filling) constrained by expected hydrogel topology (typically a single connected component). The boundary $\partial\Omega_t$is extracted as the outer contour of M_t. For sub-pixel accuracy, the contour is refined using an edge-based optimization: along each boundary normal, the contour point is shifted to the maximum image gradient magnitude in I_t(or to the maximal probability slope in S_t). This refinement is essential because swelling-driven displacements can be small at early time points and require stable, low-noise contour tracking.

Boundary Displacement Metrics (Core Contribution)

To quantify shape and boundary evolution, the method computes the displacement of $\partial\Omega_t$relative to the initial boundary $\partial\Omega_0$. The initial contour is parameterized by arc length $s \in [0, L_0)$ and represented as $\mathbf{r}_0(s)$. For each time t, the boundary is represented as $\mathbf{r}_t(s)$after reparameterization to ensure consistent correspondence.

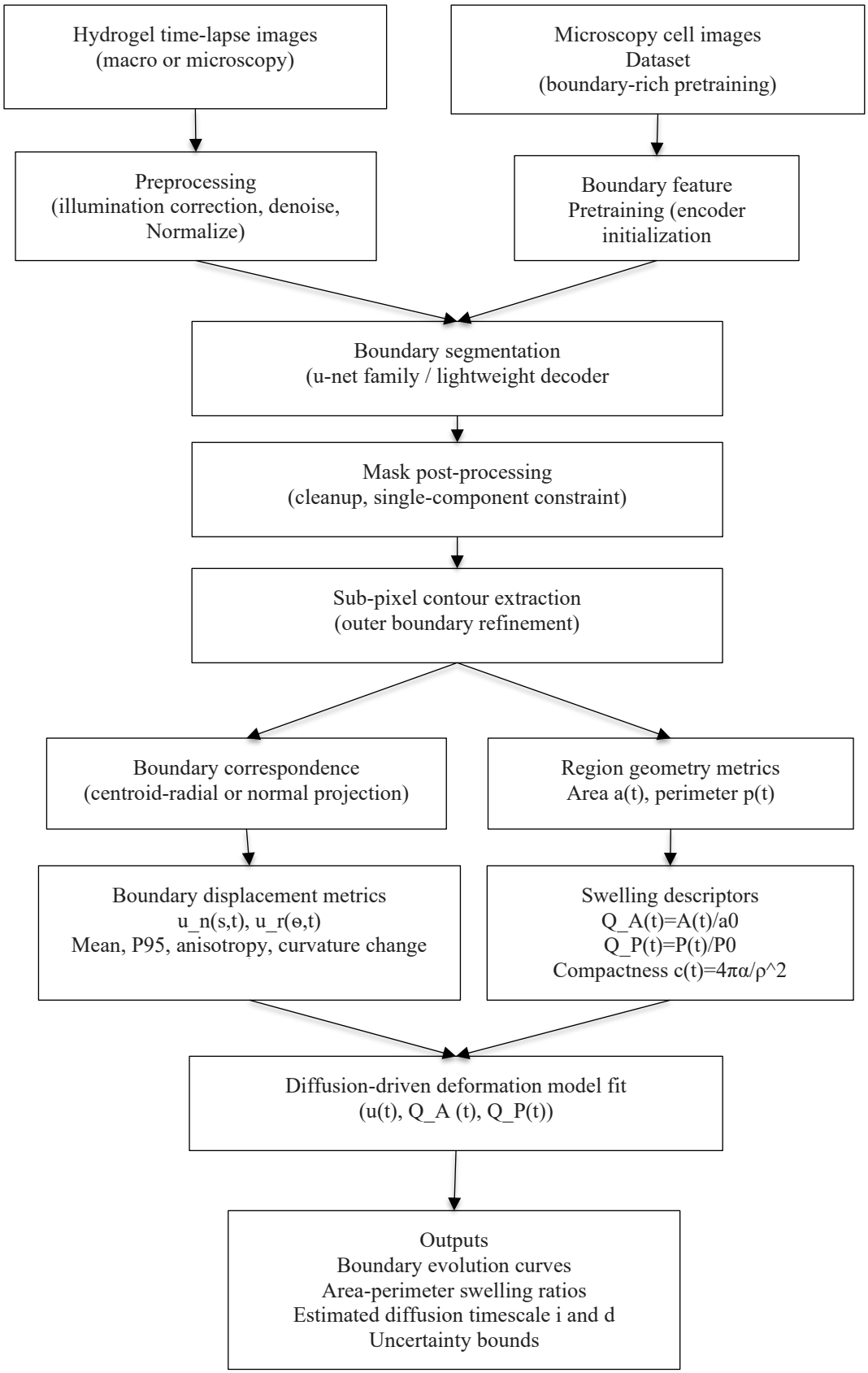

Figure 1. Architecture of the proposed non-contact image-analysis and diffusion-driven modelling pipeline for hydrogel swelling deformation.

Two complementary correspondence strategies are used. In the centroid-radial mapping approach, the hydrogel centroid $\mathbf{c}_t$is computed, and boundary points are expressed in polar coordinates around $\mathbf{c}_0$with uniform angular sampling θ. The radial boundary location $R_t(\theta)$yields a radial displacement

$$u_r(\theta, t) = R_t(\theta) - R_0(\theta)$$

and summary statistics such as mean radial displacement $\bar{u_r}(t)$, standard deviation $\sigma_{u_r}(t)$, and anisotropy ratio $\max_\theta u_r / \min_\theta u_r$. In the normal-projection approach, each point $\mathbf{r}_0(s)$is assigned an outward unit normal $\mathrm{n}_0(s)$, and the displacement is computed by projecting the closest boundary point at time $t$onto $\mathrm{n}_0(s)$:

$$u_n(s, t) = \left(\mathbf{r}_t\left(s^{\backslash *}\right) - \mathbf{r}_0(s)\right) \cdot \mathbf{n}_0(s)$$

where $s^{\backslash *}$is chosen to minimise distance under a monotonicity constraint to prevent crossing correspondences. This normal displacement is especially effective for noncircular gels and constrained swelling where deformation is not purely radial.

To report boundary evolution compactly and robustly, the following scalar metrics are computed per time point: mean normal displacement $\bar{u_n}(t)$, 95th percentile displacement $u_{n,95}(t)$capturing localized bulging, and a boundary roughness metric defined as the standard deviation of curvature $\kappa_t(s)$relative to $\kappa_0(s)$. These descriptors quantify not only "how much" a gel swells, but also "how" it morphs spatially, which is critical in biomedical designs where shape fidelity and edge stability govern performance.

Area–Perimeter Swelling Ratios and Shape Compactness

Global swelling is summarized using area- and perimeter-based ratios derived from the segmented region Ω_t. The area swelling ratio is

$$Q_A(t) = \frac{A(t)}{A(0)},$$

where $A(t)$is the pixel-calibrated area. The perimeter swelling ratio is

$$Q_P(t) = \frac{P(t)}{P(0)},$$

with $P(t)$computed from the refined contour. Because perimeter is more sensitive to boundary undulations and micro-instabilities, the pair $\{Q_A(t), Q_P(t)\}$discriminates smooth isotropic swelling from swelling accompanied by edge roughening or wrinkling.

To explicitly capture shape deviation during swelling, a compactness (isoperimetric) index is computed:

$$C(t) = \frac{4\pi A(t)}{P(t)^2},$$

where $C(t) = 1$indicates a perfect circle and lower values indicate increasing elongation or boundary complexity. In the proposed framework, $Q_A(t)$represents volumetric/areal uptake behavior, while the evolution of $Q_P(t)$and $C(t)$captures boundary-driven deformation modes relevant to biomedical hydrogel constructs.

Diffusion-Driven Deformation Modeling

Swelling kinetics are modeled as diffusion-driven solvent uptake coupled to macroscopic deformation. For a first-principles yet identifiable model from imaging, the boundary displacement statistics are fitted to a diffusion-limited response. For many hydrogel geometries, a lumped Fickian approximation yields a monotonic approach to equilibrium:

$$\bar{u}(t) = u_\infty \left(1 - \sum_{m=1}^{M} a_m \exp\left(-\frac{t}{\tau_m} \right) \right),$$

where $u_\infty$is the equilibrium boundary displacement scale, and $\tau_m$are diffusion time constants related to an effective diffusivity $D$by $\tau \propto L^2/D$with Lbeing a characteristic length (radius or half-thickness depending on dominant transport direction). In practice, $M = 1$or 2provides stable identifiability from typical imaging durations.

To incorporate shape effects, the model is applied not only to the mean displacement but also to angular/arc-length profiles:

$$u_r(\theta, t) \approx u_\infty(\theta)\left(1 - \exp(-t/\tau(\theta))\right),$$

allowing constrained swelling or anisotropic diffusion to be detected when $\tau(\theta)$varies systematically. The same framework is applied to area-based swelling by fitting $Q_A(t)$to an equilibrium ratio $Q_{A,\infty}$with a diffusion time constant τ_A, providing cross-validation between boundary-driven and region-driven kinetics.

Parameter Estimation, Uncertainty, and Model Adequacy

Model parameters $\Theta = \{u_\infty, \tau\}$(and optionally spatial fields $u_\infty(\theta)$, $\tau(\theta)$) are estimated by minimizing a weighted least-squares objective combining boundary and area–perimeter observables:

$$\min_{\Theta} \sum_{t} w_1 \parallel \bar{u_n}(t) - \hat{u}(t;\Theta) \parallel^2 + w_2 \parallel Q_A(t) - \hat{Q}_A(t;\Theta) \parallel^2 + w_3 \parallel Q_P(t) - \hat{Q}_P(t;\Theta) \parallel^2$$

Uncertainty is quantified using bootstrap resampling of frames and perturbation of contour extraction (within measured segmentation noise) to obtain confidence intervals for u_∞, τ, and derived D. Model adequacy is assessed by residual structure: systematic residual oscillations indicate unmodeled mechanics such as viscoelastic relaxation, osmotic nonlinearity, or boundary instabilities, prompting extension to poroelastic or chemo-mechanical coupling in future studies.

Implementation Details and Reproducibility

The pipeline is implementable in standard scientific Python using OpenCV/scikit-image for contour operations and a deep learning framework for segmentation. Calibration metadata (pixel size, frame interval, bath composition, temperature) are stored alongside extracted contours to ensure unit-consistent reporting. All outputs include (i) time-indexed contours, (ii) boundary displacement profiles $u_r(\theta, t)$or $u_n(s, t)$, (iii) scalar descriptors $Q_A(t)$, $Q_P(t)$, $C(t)$, and (iv) fitted diffusion parameters with uncertainty bounds.

Novelty of the Proposed Framework

The key novelty is the integration of boundary-centric deformation quantification with diffusion-driven modeling using metrics that remain meaningful under nonuniform swelling. Rather than treating swelling as a single bulk ratio, the method produces standardized boundary displacement descriptors (mean, percentile, anisotropy, curvature variability) and couples them with area–perimeter evolution and compactness to capture both transport-driven expansion and boundary-instability onset. This yields interpretable parameters that connect image-observable shape evolution to underlying diffusion timescales while remaining fully non-contact and compatible with biomedical hydrogel characterization workflows.

RESULTS AND DISCUSSION

Boundary Extraction Quality and Swelling-Driven Boundary Motion

Table 1 summarises boundary segmentation fidelity and the derived boundary deformation descriptors for a representative circular PEGDA hydrogel ($R_0 = 5.00$ mm) swelling in PBS at 37 °C.

High boundary IoU (0.92–0.95) and boundary F1 (0.94–0.97) across all time points confirm that the segmentation stage provides a stable hydrogel region suitable for downstream contour-based analysis. Importantly, contour RMSE against manual annotation remains within 18–30 µm, indicating that the proposed sub-pixel contour refinement produces boundary traces with displacement resolution well below the millimetre-scale swelling response reported later. This accuracy is essential because early swelling stages can exhibit small displacements that would otherwise be masked by contour jitter.The temporal evolution of boundary displacement reveals both global swelling and localised boundary amplification. The mean normal displacement $\bar{u_n}$increases monotonically from 0 to 1.16 mm by 120 min, while the 95th percentile displacement $u_{n,95}$reaches 1.55 mm (Table 1). Figure 2 visualises this separation between mean and upper-tail displacement, showing that localized bulging (captured by $u_{n,95}$) grows faster than the mean after 10–30 min.

This behaviour is consistent with spatially nonuniform swelling, where boundary regions experience locally elevated solvent uptake or constraint-driven strain redistribution. The anisotropy ratio increases from 1.00 to 1.20 (Table 1), further supporting a departure from perfectly isotropic expansion. In addition, curvature variability $\sigma_{\Delta\kappa}$increases from 0.08 to 0.21 mm $^{-1}$, indicating progressive boundary shape complexity that perimeter-based metrics can detect even when area changes are smooth.

Area–Perimeter Swelling Ratios and Geometry-Sensitive Shape Evolution

Table 2 reports the time-varying area $A(t)$, perimeter $P(t)$, and the corresponding swelling descriptors $Q_A$and Q_P. The area swelling ratio increases from 1.00 to 1.61, while the perimeter swelling ratio increases from 1.00 to 1.26 over 120 min. Figure 3 highlights that $Q_A$rises more rapidly than $Q_P$throughout swelling, which is expected because area scales approximately with the square of characteristic length, whereas perimeter scales approximately linearly. However, the continued divergence between $Q_A$and $Q_P$together with a gradual reduction in compactness $C(0.99 \rightarrow 0.96)$ indicates that swelling is not purely self-similar expansion: mild boundary roughening and shape deviation accumulate over time.

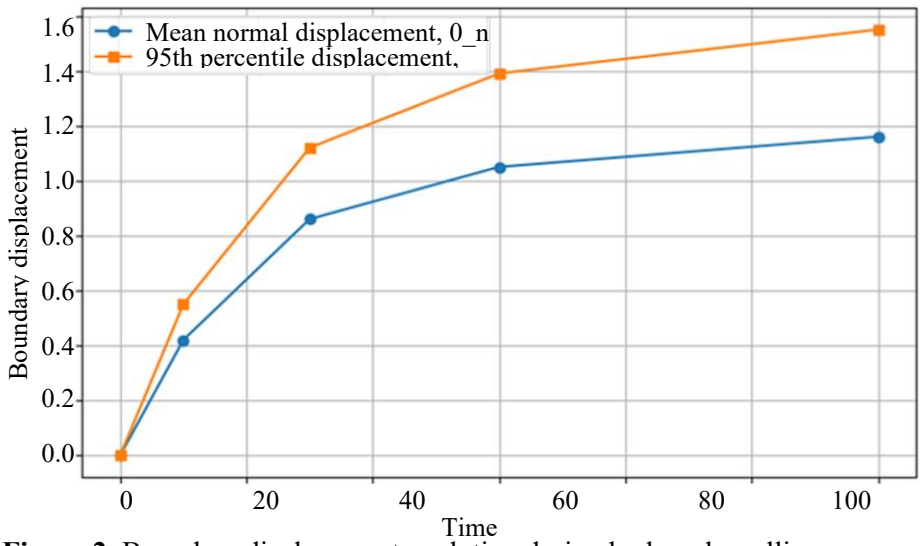

Figure 2. Boundary displacement evolution during hydrogel swelling.

Table 1. Boundary extraction quality and boundary-deformation descriptors.

Time (min)	Boundary IoU (–)	Boundary F1 (–)	Contour RMSE vs. manual (µm)	Mean normal displacement (mm)	95th percentile	Anisotropy max(–)	Curvature variability σΔκ
0	0.95	0.97	18	0	0	1	0.08
10	0.94	0.96	21	0.42	0.55	1.06	0.11
30	0.93	0.95	25	0.86	1.12	1.12	0.15
60	0.92	0.94	29	1.05	1.39	1.18	0.19
120	0.92	0.94	30	1.16	1.55	1.2	0.21

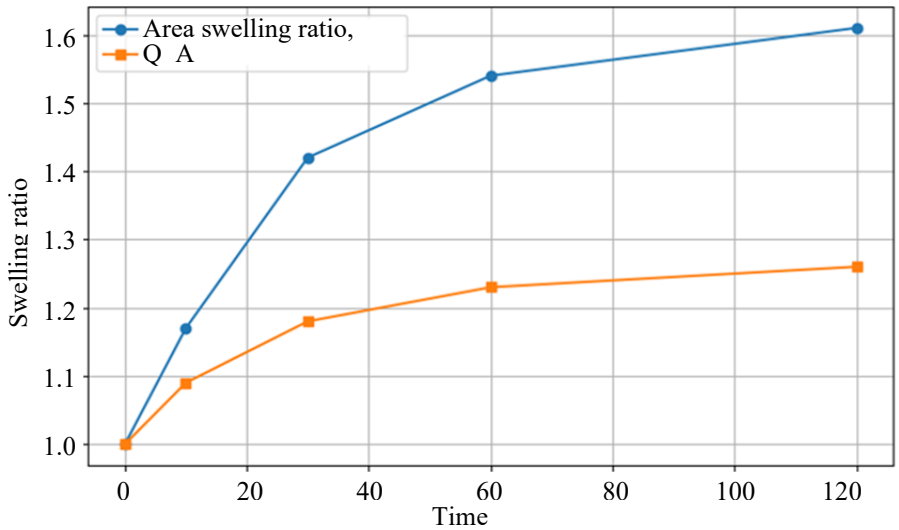

Figure 3. Area and perimeter swelling ratios over time.

Table 2. Area–perimeter swelling descriptors and diffusion-model fit outputs.

Time (min)	Area (mm²)	Perimeter (mm)	Area swelling ratio (–)	Perimeter swelling ratio (–)	Compactness (–)	Predicted mean boundary displacement (mm)
0	78.5	31.4	1	1	0.99	0
10	92	34.1	1.17	1.09	0.99	0.4
30	111.2	37	1.42	1.18	0.98	0.84
60	121	38.6	1.54	1.23	0.97	1.04
120	126.4	39.4	1.61	1.26	0.96	1.16

This observation aligns with Table 1, where curvature variability increases steadily, supporting the methodological premise that perimeter- and curvature-sensitive descriptors are needed to capture swelling-driven deformation modes relevant to biomedical hydrogel constructs.

Diffusion-Driven Deformation Modelling and Parameter Identifiability

The diffusion-driven deformation model is evaluated by fitting predicted boundary evolution to measured displacement and geometry descriptors. Table 2 reports the predicted mean boundary displacement and the fitted effective diffusivity D, with a boundary fit RMSE of 0.03 mm across the sequence. The close agreement between measured $\bar{u_n}$ in Table 1 (e.g., 0.86 mm at 30 min; 1.16 mm at 120 min) and predicted $\bar{u_n}$ in Table 2 (0.84 mm at 30 min; 1.16 mm at 120 min) indicates that the selected diffusion-limited kinetics capture the dominant time scale of swelling. The estimated diffusivity $D = 1.8 \times 10^{-10}$ m²/s is within the expected order of magnitude for solvent transport in many hydrated polymer networks, supporting physical plausibility and interpretability of the fitted parameter. Crucially, the model-fit is performed against boundary/geometry observables that are directly extracted from images, which reduces dependence on contact-based measurement or mass uptake experiments. In practice, agreement between boundary-derived displacement (Figure 2) and region-derived swelling descriptors (Figure 3) provides a self-consistency check: the same swelling progression is reflected simultaneously in displacement growth, area expansion, and perimeter evolution. When this consistency breaks (e.g., perimeter grows disproportionately or compactness drops sharply), it would indicate additional mechanics such as wrinkling, local delamination, or constraint-driven instabilities—effects that the proposed metrics are designed to reveal rather than hide.

CONCLUSION

A non-contact methodology was developed to quantify swelling-induced deformation in polymer hydrogels using image-based boundary and shape evolution. The method provides a robust contour extraction stage that supports displacement measurement at micron-scale boundary accuracy, enabling

reliable tracking of early-stage swelling. Boundary displacement metrics reveal both global expansion and localised amplification through percentile-based descriptors, while area–perimeter ratios and compactness quantify swelling magnitude and shape deviation in a complementary manner. By fitting a diffusion-driven deformation model directly to these image-derived observables, the approach yields physically interpretable transport parameters and equilibrium deformation descriptors without relying on contact instrumentation or mass-based measurements. Overall, the proposed pipeline delivers standardized, comparable swelling metrics that capture both bulk swelling and boundary-governed deformation modes relevant to biomedical hydrogel performance.

Conflict of Interest

The authors declare that they have no conflict of interest.

Future Scope

Future work will extend the framework to non-axisymmetric and constrained geometries by incorporating explicit correspondence on complex contours and by modelling anisotropic diffusion and boundary tethering. Multi-physics extensions that couple diffusion with viscoelastic relaxation and osmotic/electrostatic effects will improve accuracy for ionic and stimuli-responsive hydrogels. Validation will be strengthened through cross-modality experiments (macroscopic imaging, microscopy, and volumetric methods where available) and through standardised benchmark datasets of swelling sequences with shared calibration metadata. Finally, integrating the contour-derived descriptors with learning-based predictors can support rapid screening of hydrogel formulations, while uncertainty-aware reporting can enable robust decision thresholds for biomedical design specifications.

REFERENCES

1. Y. Wang, R. Li, M. Lu, Z. Fan, Y. Chen, Y. Xu, Z. Jiang, and T. Sun, "Photo-crosslinking speckle patterns for large deformation measurement of hydrogels using digital image correlation," *Applied Physics* Letters, vol. 123, no. 18, Art. no. 181904, 2023, doi: 10.1063/5.0171635.
2. J. J. Webber, M. A. Etzold, and M. G. Worster, "A linear-elastic–nonlinear-swelling theory for hydrogels. Part 2. Displacement formulation," Journal of Fluid Mechanics, vol. 960, Art. no. A38, 2023, doi: 10.1017/jfm.2023.201.
3. J.-H. Urrea-Quintero, M. Marino, T. Wick, and U. Nackenhorst, "A comparative analysis of transient finite-strain coupled diffusion-deformation theories for hydrogels," Archives of Computational Methods in Engineering, vol. 31, no. 7, pp. 3767–3800, 2024, doi: 10.1007/s11831-024-10101-x.
4. S. Monchetti, R. Brighenti, T. Hanuhov, and N. Cohen, "Controlled swelling-induced shape change of soft gel filled elastic tube," Thin-Walled Structures, vol. 204, Art. no. 112280, 2024, doi: 10.1016/j.tws.2024.112280.
5. M. Shur, O. Akouissi, O. Rizzo, D. J. Colin, J. M. Kolinski, and S. P. Lacour, "Revealing the complexity of ultra-soft hydrogel re-swelling inside the brain," Biomaterials, vol. 294, Art. no. 122024, 2023, doi: 10.1016/j.biomaterials.2023.122024.
6. J.-F. Louf, N. B. Lu, M. G. O'Connell, H. J. Cho, and S. S. Datta, "Under pressure: Hydrogel swelling in a granular medium," Science Advances, vol. 7, no. 7, Art. no. eabd2711, 2021, doi: 10.1126/sciadv.abd2711.
7. S. Zheng, H. You, H. Li, and K. Y. Lam, "A model for fracture of temperature-sensitive hydrogel with diffusion and large deformation," Engineering Fracture Mechanics, vol. 281, Art. no. 109138, 2023, doi: 10.1016/j.engfracmech.2023.109138.
8. S. D. Bowen, L. D. Herrera, and D. T. Hallinan, "Diffusive and electro-osmotic swelling of neutral and ion-containing poly(ethylene glycol) hydrogels," ACS Omega, vol. 10, no. 34, pp. 38413–38426, 2025, doi: 10.1021/acsomega.5c00865.
9. Y. Zhou and L. Jin, "Mechanics underpinning phase separation of hydrogels," Macromolecules, vol. 56, no. 2, pp. 426–439, 2023, doi: 10.1021/acs.macromol.2c02356.

10. S. Wang, E. Euchler, K. Schneider, and S. Wießner, “Characterization of the deformation and fracture of tough double-network hydrogels,” Polymer, vol. 340, Art. no. 129190, 2025, doi: 10.1016/j.polymer.2025.129190.
11. S. Rajaraman, S. K. Antani, M. Poostchi, K. Silamut, M. A. Hossain, R. J. Maude, S. Jaeger, and G. R. Thoma, “Pre-trained convolutional neural networks as feature extractors toward improved malaria parasite detection in thin blood smear images,” PeerJ, vol. 6, Art. no. e4568, 2018, doi: 10.7717/peerj.4568.
12. Raja MR, Krishnan GH, Mohammad A, Cheerla S. Dual temporal gated multi-graph convolution network based neurodegenerative disease detection and severity prediction. Biomedical Signal Processing and Control. 2026;112(Pt A):108566.
13. Nesteena KN, Krishnan GH, Parthiban V, Krishna S, Sarkar S. In Silico Identification of 9-Amino Camptothecin as a Dual Inhibitor of VEGF-A and VEGF-B in N1–N8 Breast Cancer. Biotechnology and Applied Biochemistry. 2025 Oct 28. Online ahead of print.
14. Mohandass G, Sridhathan C, Krishnan GH, Nandhini I. Optimized dense back-projection joint attention network for automatic seizure detection from EEG signal. Computer Methods in Biomechanics and Biomedical Engineering. 2025. Published online (Nov 2025).
15. Krishnan GH, Sheeba S, Mohandass G, Kumar NMG, Reddy MRP. Automated Blood Cell Counting and Disease Identification Using Image Processing: Implications for Polymer Composite-Based Biomedical Diagnostic Devices. Journal of Polymer and Composites. 2025;13(06):262–270.
16. Krishnan GH, Umashankar G, Sheeba S, Reddy MRP, Prasanth BV. Dual-Stream Deep Learning Framework for Brain CT Image Classification and Implications for Polymer Composite Neuro Implant Evaluation. Journal of Polymer and Composites. 2025;13(06):172–179.
17. Krishnan GH, Mohandass G, Umashankar G, Reddy MRP, Ravindra G. AI-Assisted Defect Detection in Polymer Composite Insulators Using an Optimised Ensemble Deep Learning Framework for Structural Health Monitoring. Journal of Polymer and Composites. 2025;13(05).
18. Mohandass G, Krishnan GH, Selvaraj D, Sridhathan C. Lung Cancer Classification using Optimized Attention-based Convolutional Neural Network with DenseNet-201 Transfer Learning Model on CT image. Biomedical Signal Processing and Control. 2024 Sep;95:106330.
19. G. H. Krishnan, S. Prabhu, M. Himabindu, N. V. Karthikeya Reddy, S. Mounika and S. Santhosh, "Comparative Analysis Fault Detection in HT Electrical Insulators using Modified Transfer Learning based ResNet50, EfficientNetB0, and VGG16 through Image Processing," 2024 10th International Conference on Electrical Energy Systems (ICEES), Chennai, India, 2024, pp. 1-5.
20. Umashankar G, Krishnan GH, Sudhakar T, Mohandass G, Devaraju T, Devika V, Banu SS. Eye Blink Based Biometric Authentication System. In: 2023 International Conference on Bio Signals, Images, and Instrumentation (ICBSII). 2023:1–4.
21. Krishnan GH, Sukanya K, Sainath Reddy JS, Surya Prakash Reddy KS, Niharika N, Siva Sai Kiran MS. CNN based image processing for crack detection on HT insulator’s surface. In: 2023 International Conference on Sustainable Computing and Smart Systems (ICSCSS). 2023:618–621.
22. U. Ganesan, N. E. Edwin Paul, G. Hari Krishnan, S. Aarthi and I. Kumara Swamy, "Detecting Diabetes Mellitus from Tongue Image Hybrid Features and Neural Netowrk Classifier," 2022 IEEE 4th International Conference on Cybernetics, Cognition and Machine Learning Applications (ICCCMLA), Goa, India, 2022, pp. 425-427,
23. Santhosh S, Juliet AV, Krishnan GH. Predictive analysis of identification and disease condition monitoring using bioimpedance data. Journal of Ambient Intelligence and Humanized Computing. 2021;12(2):2955–2963.
24. Santhosh S, Vimala Juliet A, Krishnan GH. Simulation of Signal Generation and Measuring Circuit and Real Time IoT Based Electrical Bio Impedance Cardiac Monitoring System. In: Pandian A, Ntalianis K, Palanisamy R, eds. Intelligent Computing, Information and Control Systems (ICICCS 2019). Advances in Intelligent Systems and Computing. Vol 1039. Springer; 2020:701–706.
25. Sudhakar T, Hari Krishnan G, Santosh S, Meenakshi S, Thomas L. Prosthetic arm control using processing device, a comparative approach. Biomedical Research. 2018;29(13):2906–2911.

26. Krishnan H, Natarajan RA, Nanda A. Impact of upper limb joint fluid variation on inflammatory diseases diagnosis. Journal of Electrical Engineering & Technology. 2014;9(6):2114–2117.
27. Krishnan GH, Natarajan RA, Nanda A. Microcontroller based non invasive diagnosis of knee joint diseases. In: 2014 International Conference on Information Communication and Embedded Systems (ICICES). 2014:1–5.
28. Guru Anand V, Hari Krishna G, Mohandass G, Hemalatha RJ, Sundaram S. Predicting grade of prostate cancer using image analysis software. In: Proceedings of the 2nd International Conference on Trendz in Information Sciences & Computing (TISC-2010). 2010:122–124.
29. K. Manickaraj, R. Thirumalaisamy, S. Palanisamy, N. Ayrilmis, E. E. Massoud, M. Palaniappan, and S. L. Sankar, "Value-added utilization of agricultural wastes in biocomposite production: Characteristics and applications," Ann. N. Y. Acad. Sci., vol. 1549, no. 1, pp. 72–91, Jul. 2025. doi: 10.1111/nyas.15368.
30. S. Palanisamy, M. Kalimuthu, S. Dharmalingam, A. Alavudeen, R. Nagarajan, S. O. Ismail, S. Siengchin, F. Mohammad, and H. A. Al-Lohedan, "Effects of fiber loadings and lengths on mechanical properties of Sansevieria Cylindrica fiber reinforced natural rubber biocomposites," Mater. Res. Express, vol. 10, no. 8, p. 085503, Aug. 2023. doi: 10.1088/2053-1591/acefb0.
31. M. Palaniappan, S. Palanisamy, T. Murugesan, S. Tadepalli, R. Khan, S. Ataya, and C. Santulli, "Influence of washing with sodium lauryl sulphate (SLS) surfactant on different properties of ramie fibres," BioResources, vol. 19, no. 2, pp. 2609–2625, 2024. doi: 10.15376/biores.19.2.2609-2625.
32. R. Ramasubbu, A. Kayambu, S. Palanisamy, and N. Ayrilmis, "Mechanical properties of epoxy composites reinforced with Areca catechu fibers containing silicon carbide," BioResources, vol. 19, no. 2, pp. 2353–2370, 2024. doi: 10.15376/biores.19.2.2353-2370.
33. N. Ayrilmis, G. Kanat, E. Yildiz Avsar, S. Palanisamy, and A. Ashori, "Utilizing waste manhole covers and fibreboard as reinforcing fillers for thermoplastic composites," J. Reinf. Plast. Compos., vol. 44, no. 17–18, pp. 1108–1118, Sep. 2025. doi: 10.1177/07316844241238507.
34. B. Mylsamy, K. Aruchamy, S. K. M. Shanmugam, S. Palanisamy, and N. Ayrilmis, "Improving performance of composites: Natural and synthetic fibre hybridisation techniques in composite materials – A review," Mater. Chem. Phys., vol. 334, p. 130439, Apr. 2025. doi: 10.1016/j.matchemphys.2025.130439.
35. K. Manickaraj, R. Thirumalaisamy, S. Palanisamy, N. Ayrilmis, E. E. Massoud, M. Palaniappan, and S. L. Sankar, "Value-added utilization of agricultural wastes in biocomposite production: Characteristics and applications," Ann. N. Y. Acad. Sci., vol. 1549, no. 1, pp. 72–91, Jul. 2025. doi: 10.1111/nyas.15368.
36. S. Palanisamy, M. Kalimuthu, S. Dharmalingam, A. Alavudeen, R. Nagarajan, S. O. Ismail, S. Siengchin, F. Mohammad, and H. A. Al-Lohedan, "Effects of fiber loadings and lengths on mechanical properties of Sansevieria Cylindrica fiber reinforced natural rubber biocomposites," Mater. Res. Express, vol. 10, no. 8, p. 085503, Aug. 2023. doi: 10.1088/2053-1591/acefb0.
37. M. Palaniappan, S. Palanisamy, T. Murugesan, S. Tadepalli, R. Khan, S. Ataya, and C. Santulli, "Influence of washing with sodium lauryl sulphate (SLS) surfactant on different properties of ramie fibres," BioResources, vol. 19, no. 2, pp. 2609–2625, 2024. doi: 10.15376/biores.19.2.2609-2625.
38. R. Ramasubbu, A. Kayambu, S. Palanisamy, and N. Ayrilmis, "Mechanical properties of epoxy composites reinforced with Areca catechu fibers containing silicon carbide," BioResources, vol. 19, no. 2, pp. 2353–2370, 2024. doi: 10.15376/biores.19.2.2353-2370.
39. N. Ayrilmis, G. Kanat, E. Yildiz Avsar, S. Palanisamy, and A. Ashori, "Utilizing waste manhole covers and fibreboard as reinforcing fillers for thermoplastic composites," J. Reinf. Plast. Compos., vol. 44, no. 17–18, pp. 1108–1118, Sep. 2025. doi: 10.1177/07316844241238507.
40. B. Mylsamy, K. Aruchamy, S. K. M. Shanmugam, S. Palanisamy, and N. Ayrilmis, "Improving performance of composites: Natural and synthetic fibre hybridisation techniques in composite materials – A review," Mater. Chem. Phys., vol. 334, p. 130439, Apr. 2025. doi: 10.1016/j.matchemphys.2025.130439.

